Motor-Like Properties of Non-Motor Enzymes

David R. Slochower[1] and Michael K. Gilson[1*]

Affiliations:

[1] Skaggs School of Pharmacy and Pharmaceutical Sciences, University of California San Diego, La Jolla, California 92093-0736, United States.

*Correspondence to: mgilson@ucsd.edu.

Abstract: Biological molecular motors use chemical free energy to drive mechanical motion in a specific direction. This function appears to require high molecular complexity, and it is interesting to consider how the evolutionary leap from non-motor enzymes to molecular motors occurred. Here, atomistic simulations coupled with kinetic modeling show that conformational switching of non-motor enzymes, induced by substrate binding and catalysis, induces motor-like, directional torsional motions, as well as oar-like, reciprocating motions, which should be detectable experimentally. Such directional motions in the earliest enzymes would have been starting point for the evolution of motor proteins. Additionally, driven molecular motions in catalytically active enzymes may help explain why the apparent diffusion constants of some enzymes increase with enzyme velocity (*1-3*).

One Sentence Summary: Analysis of protein simulations shows that catalytically active non-motor enzymes can execute motor-like motions.

Main Text:

A biological molecular motor is an enzyme that uses the free energy of an out-of-equilibrium chemical reaction to drive mechanical motion. This motion must have a specific direction to fulfill the motor's functional role; for example, a helical flagellum must rotate in the appropriate sense to propel the organism. The ability to generate directional motion may appear to be a complex protein property, so it is interesting to consider how non-motor enzymes could have evolved to molecular motors. Here, we use computational and theoretical methods to test a hypothesis that essentially any enzyme catalyzing an out-of-equilibrium reaction executes directional motions. The results bear on motor evolution, the importance of chirality, and recent experimental observations of enzyme diffusion and motility.

When an enzyme binds a molecule of substrate and catalyzes its conversion to product, it switches stochastically between two distinct conformational free energy surfaces, one for the apo state and one for the substrate-bound state. We used the flashing potential model (*4-6*), which has previously been used to understand the mechanisms of molecular motors (*7-11*), to compute the dynamical consequences of this switching, based on known enzyme kinetic parameters and energy profiles of the two surfaces derived from simulations. The one-dimensional free energy surfaces of protein main- and side-chain torsions, discretized into bins, were obtained from detailed equilibrium molecular dynamics (MD) simulations of enzymes in their apo and substrate-bound states (Supplementary Methods). These data, coupled with literature values for the enzyme kinetic parameters (Table S1), enabled us to define first order rate constants for transitions along and between the free energy surfaces (Fig. S1). The resulting set of rate equations was solved for the non-equilibrium steady state probability distribution and this, in turn, was used to compute the probability flux on each surface. The net flux, J, in units of torsional rotational cycles per second, is an indication of directional rotation; e.g., a positive value implies clockwise rotation of the torsion.

We used this method to analyze motions in three enzymes, each with distinctive characteristics: adenylate kinase (ADK), with 214 residues and a relatively high k_{cat} ~300 s^{-1} (*12, 13*), undergoes extensive conformational change on binding substrate, with two domains reorienting to form a compact conformation (*14, 15*); protein kinase A (PKA), with 350 residues and k_{cat} ~140 s^{-1} (*16*), acts as a "dynamic switch", with long-range allosteric interactions and domain rearrangement upon ligand binding (*17*); while HIV-1 protease (HIVP), with 200 residues and lower k_{cat} ~10 s^{-1}

(*18-20*), contains two flexible flaps that lose mobility in the substrate-bound state (*21, 22*) (Fig. S2).

For all three enzymes, the present model indicates that multiple torsion angles undergo directional rotations, as indicated by nonzero torsional fluxes, when excess substrate is present. Thus, at high substrate concentration, about 40 torsions in ADK and PKA are found to rotate faster than 10 cycle s^{-1}, and about 140 are found to rotate faster than 1 cycle s^{-1} (Fig. 1a). The corresponding numbers are lower for HIVP (Fig. 1b, red), but this largely reflects the lower k_{cat} value of HIVP versus PKA (*16, 23*) and ADK (*12, 13*), because artificially assigning $k_{cat} = 200\ s^{-1}$ to HIVP leads to substantial increases in the number of torsions with fluxes of at least 10 s^{-1} and at least 1 s^{-1} (Fig. 1b, orange and Fig. S4). The tendency toward lower fluxes in HIVP may also reflect the smaller scale of its conformational changes (Fig. S2). Although the maximum rotation rates are quite different for ADK, PKA and HIVP (180, 70 and 0.18 cycles s^{-1}, respectively), the maximum numbers of rotations per catalytic step are similar, at 0.5 – 0.6 cycles/catalytic turnover (Fig. 2). This ratio is akin to a 2:1 gearing of catalysis to torsional rotation. (Figure S3 provides further details regarding the relationships between catalytic rate and torsional flux for additional torsions.) The angles with directional flux are distributed throughout the proteins' structures, with high flux torsions localized near the substrate binding pocket or mobile regions (Fig. S2).

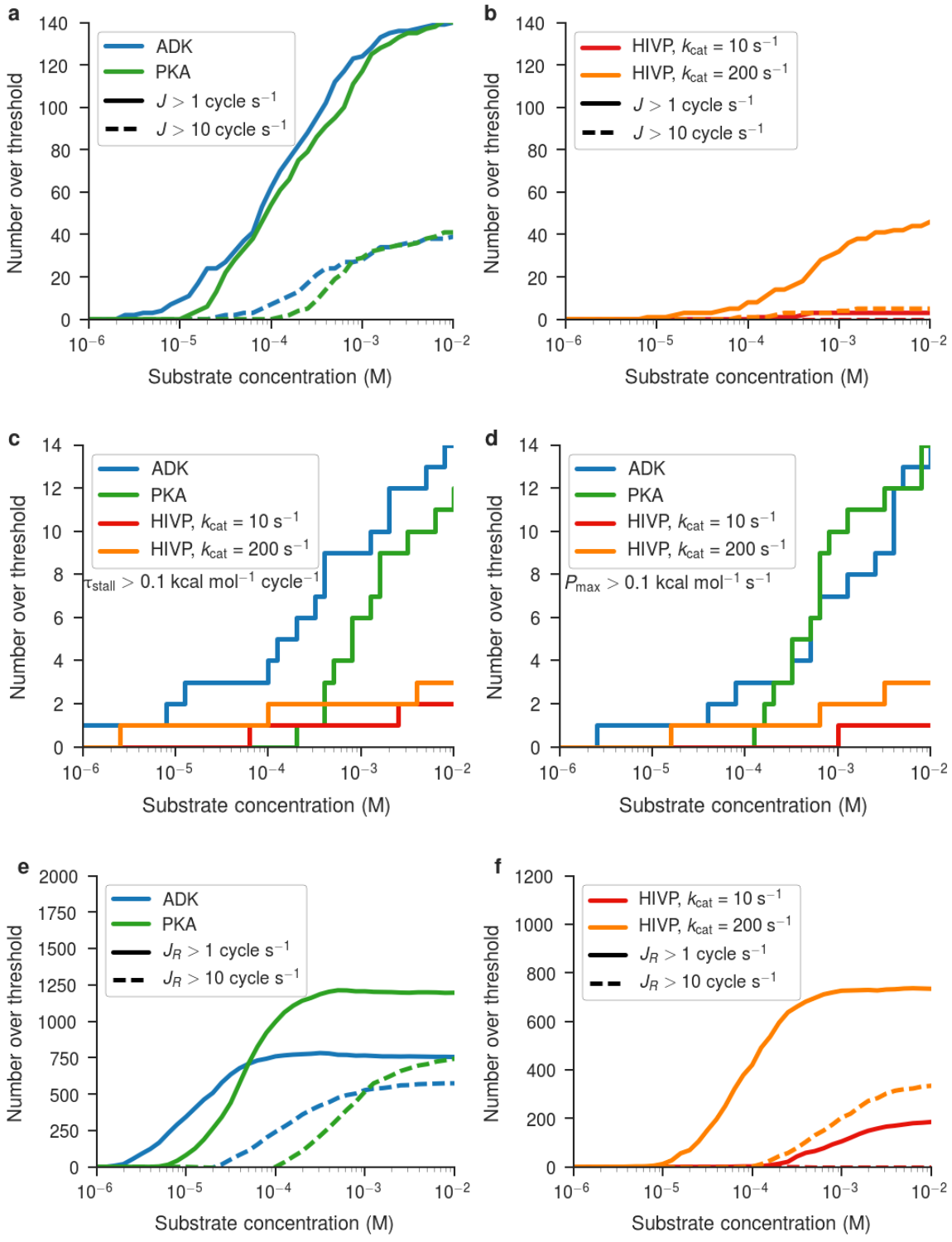

Fig. 1. The number of torsions above various thresholds of directional flux magnitude, reciprocating flux magnitude, stall torque, and maximum power, as a function of substrate concentration. (a-b) The number of torsions with directional flux above 1 (solid) or 10 (dotted) cycle s^{-1} in ADK, PKA, and HIVP. (c-d) The number of angles with (c) maximum stall force above 0.1 kcal/(mol·cycle) and (d) power above 0.1 kcal/(mol·s^{-1}). (e-f) The number of torsions

with reciprocating flux above 1 (solid) or 10 (dotted) cycle s^{-1} and, at the same time, directional flux less than 1 cycle s^{-1}.

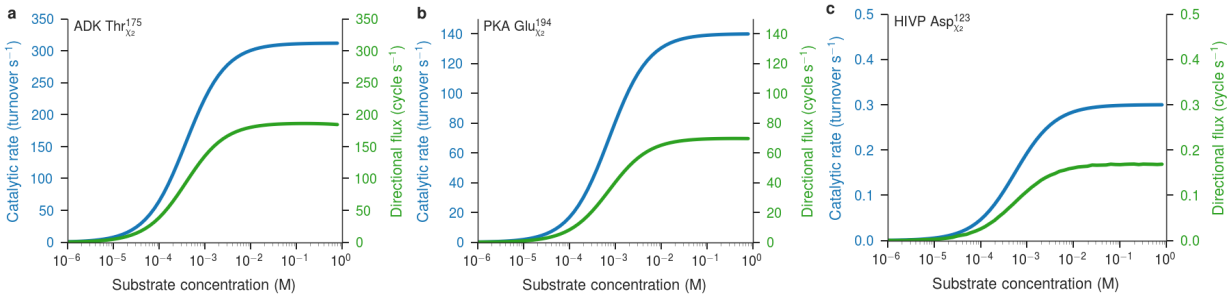

Fig. 2. Dependence of catalytic rates and of the magnitude of directional flux on substrate concentration, for torsion angles in each enzyme. (a) The χ_2 angle of Thr175 in ADK reaches a high level of directional flux. (b) The χ_2 angle of Glu194 in PKA reaches a moderate level of directional flux. (c) Although the total amount of flux in the χ_2 angle of Asp123 in HIVP is low, the ratio of directional flux to the enzyme velocity is similar to that in ADK and PKA.

We furthermore evaluated power output and performance under load by tilting the energy surfaces to generate a torque, τ, opposite to the directional flux, which modifies the intrasurface bin-to-bin rate constants. The power output is the product of imposed torque and flux: $P = \tau J$. Both the maximum power and the stall torque, τ_{stall}, which brings the directional flux to zero, were found by scanning across values of applied torque. The results indicate that torsions in these enzymes can do work against small mechanical loads and thus generate power (Fig. 1c,d). In particular, at high substrate concentrations, torsions in ADK and PKA are predicted to generate stall torques up to 2.4 and 1.6 kcal mol^{-1} $cycle^{-1}$, respectively, and maximum power outputs per torsion of 70 and 28 kcal mol^{-1} s^{-1}; again, the numbers are smaller for HIVP.

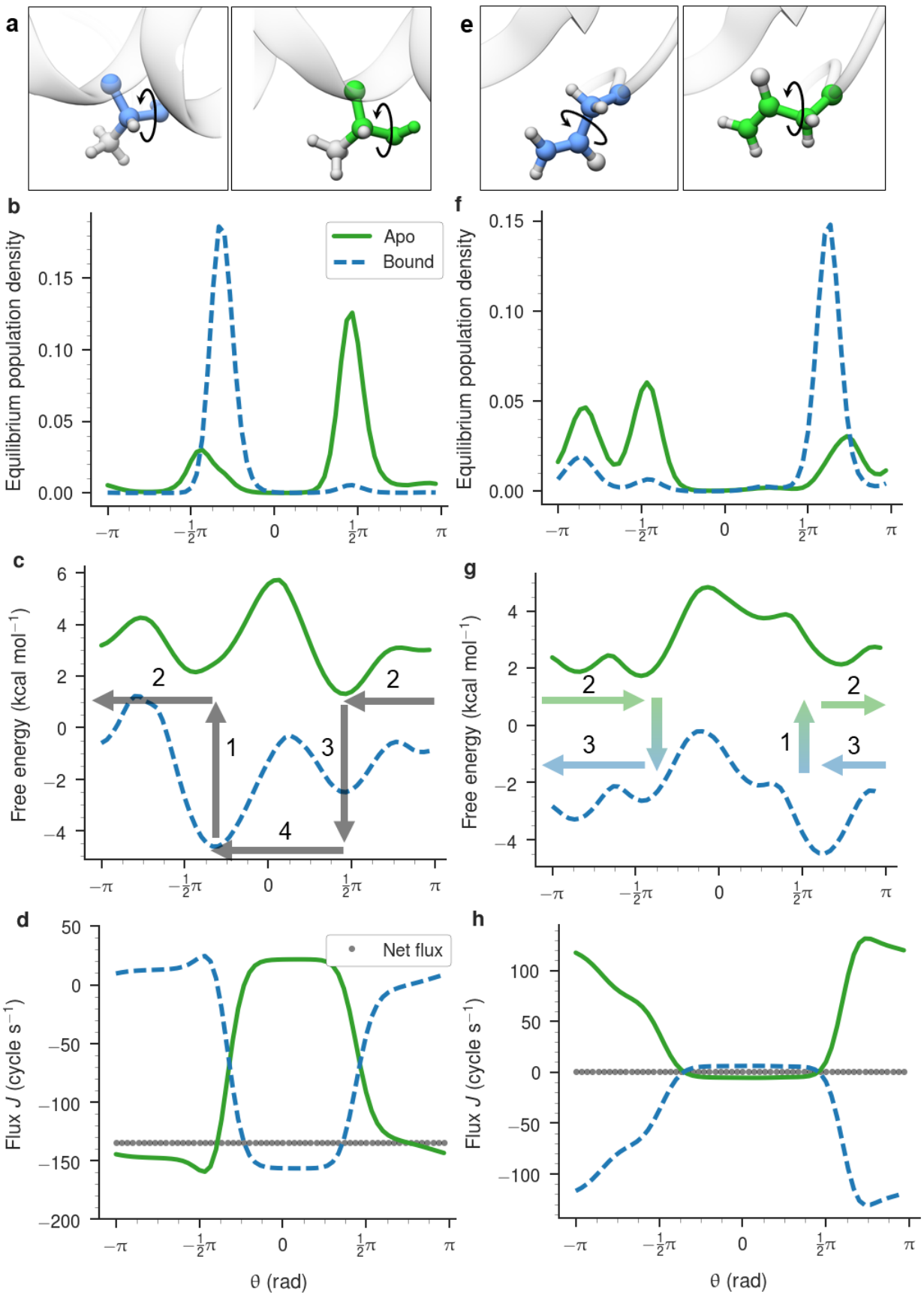

Fig. 3 Protein torsion angles show directional and reciprocating motion. (a) ADK Thr175 in its crystallographic conformations for the apo (green) and bound (blue) forms (see Supplementary Methods for PDB accessions) with the χ_2 angle denoted. The coloring is the same for panels a through d. (b) Equilibrium population densities of this angle from MD simulations (Supplementary Methods). (c) Free energy surfaces of this angle (Supplementary Methods) derived from the population densities in panel b. Arrows indicate the direction of probability flux along, and between, the two surfaces. (d) The probability flux drawn separately for each surface and as a sum (grey points), indicating large directional and reciprocating fluxes. (e-h) Same as a-d for ADK Asn138. In all cases the substrate concentration is 10^{-3} M.

The mechanism by which directional rotation is generated is illustrated by the χ_2 torsion of ADK Thr175 (Fig. 3a). This angle has a two-peaked probability distribution in both the bound and apo states, but the peak near $+\frac{\pi}{2}$ is favored in the apo state, while that near $-\frac{\pi}{2}$ is favored in the bound state (Fig. 3b,c). In the presence of substrate, the bound-state energy minimum near $-\frac{\pi}{2}$ is highly occupied (Fig. 3b,c). Catalytic breakdown of substrate pumps the system to the secondary energy minimum of the apo state at $-\frac{\pi}{2}$ (Fig. 3c, arrow 1). Probability then flows primarily to the left on the apo surface, because this is the lowest-barrier path to the apo state's global energy minimum near $+\frac{\pi}{2}$ (arrow 2; this flux goes through the periodic boundary at $\theta = -\pi \equiv +\pi$). Probability pooled in the global energy minimum of the apo state near $+\frac{\pi}{2}$, then flows primarily to the bound state, by binding substrate and landing in the secondary energy minimum of the bound state (arrow 3). It then flows back to the global minimum of the bound state via the lowest-barrier path, which is again leftward (arrow 4). The net effect is a leftward flux of up to -140 cycles s^{-1}. Fig. 1d shows the steady state flux on each surface: leftward flux predominates overall, but occurs on the apo surface between $-\frac{\pi}{2}$ to $+\frac{\pi}{2}$, and on the bound surface elsewhere, with crossovers between surfaces at the energy minima. This process parallels flashing potential mechanisms previously invoked to explain highly evolved molecular motors (*6, 7, 10, 11, 24-27*).

It is worth emphasizing that this mechanism can operate only if the molecule is chiral; otherwise, the two rotational directions would be indistinguishable. In addition, it is the thermodynamically favorable catalytic dissociation of substrate, which throws the system from the bound to the apo surface, that drives the whole process. Importantly, the substrate need not be ATP: any substrate will do, if the concentrations of substrate and product position the chemical system away from equilibrium.

In addition to torsions with significant directional flux, many torsions with minimal directional flux (<1 cycle s^{-1}) nonetheless undergo large reciprocating fluxes, corresponding to driven oar-like motions. These are torsions having an angular range within which clockwise motion occurs on one surface (e.g., bound) and counterclockwise motion occurs on the other surface (e.g., apo). Indeed, ADK and PKA are predicted to have ~1250 and ~750 torsions with minimal directional flux, but with reciprocating motions at rates of at least 1 cycle s^{-1} (Fig. 1e,f). The maximal reciprocating fluxes are greater than the maximal directional fluxes, and, for ADK and PKA, are essentially equal to the catalytic rates (Fig. S3). The mechanism by which reciprocating motion is generated is illustrated by χ_2 of Asn 138 in ADK (Fig. 3e), which has near-zero net flux but undergoes cycles of driven, reciprocating flux, with intrasurface fluxes reaching 130 cycles s^{-1} (Fig. 3e-h).

Thus, enzymes not normally regarded as motor proteins have motor-like properties: in the presence of excess substrate, they exhibit not only driven reciprocating motions but also directional rotation. The present findings for ADK, PKA, and HIVP furthermore generalize in

two ways. First, the flashing ratchet model implies that any chiral molecule that is switched back and forth between two energy surfaces is expected to undergo directional rotation, unless it is blocked by a high energy barrier, based on the following reasoning. After the energy surface is switched, the chiral asymmetry of the new energy surface means that probability will flow more in one direction than the other; and, when the surface is switched back again, a second directional probability flow occurs, on the other energy surface, and only by coincidence will the two probability flows cancel perfectly. The imbalance between the two flows represents net rotation. Note that that the two directions of rotation would be indistinguishable if the molecule were not chiral; in this case, these directional motions would not occur. Thus, chiral molecules may have been favored by natural selection due to their special ability to generate directional motion.

Second, although this study focuses on torsional motions, analogous reasoning applies to motions through higher-order conformational subspaces. For example, if an enzyme's chemical reaction is out of equilibrium, the opening and closing motions of its active site are expected to follow distinct paths, exhibiting hysteretic cycling. The hydrodynamic coupling of such hysteretic concerted motions with solvent might help explain why some enzymes diffuse faster when catalytically active (*1-3, 28, 29*). Moreover, because hysteretic motions are exempt from the scallop theorem (*30*), enzymes undergoing such motions would tend to "swim" in a preferred direction within the molecular frame of reference. Therefore, they should exhibit translational drift in a preferred lab-frame direction, if they are sufficiently well aligned by, for example, a strong magnetic field or by weak association with an oriented surface or fiber. Experiments seeking such drift would serve to test the present results.

The generality of these mechanisms means that even enzymes from earliest evolutionary time would have had the ability to generate directional motion, and thus could have embarked on an evolutionary path to today's motor proteins.

Supplementary Materials:

Materials and Methods

Figures S1 – S4.

Tables S1 – S2.

References (31 -- 45)

Supplementary Materials:

Supplementary Text

Flashing potential kinetic model

Macrostates, microstates, and energy surfaces

The enzyme can exist in two macrostates, apo (P_0) or substrate-bound (P_1), and is assumed to follow Michaelis-Menten kinetics:

$$P_0 + \text{substrate} \underset{k_{off}}{\overset{k_{on}}{\underset{\text{dissociation}}{\overset{\text{association}}{\rightleftharpoons}}}} P_1 \xrightarrow[k_{cat}]{\text{catalysis}} P_0 + \text{product}$$

Thus, the substrate-bound protein can reach the apo state either through dissociation of the substrate or through catalytic conversion of the substrate into the product. The substrate concentration is held constant at a selected value, and for simplicity, the concentration of product is considered low enough that the reverse reaction makes no significant contribution to the kinetics.

The equilibrium probability distribution functions of each torsion angle of interest, in protein states P_0 and P_1, were obtained as follows. The 60-bin torsional histograms obtained from the equilibrium MD simulations described above were converted to probabilities by normalization. The resulting probability distributions were smoothed with a Gaussian kernel (standard deviation of 1 bin), and any bins with zero probability after smoothing were assigned the lowest probability observed in any bin for that angle (typically about 10^{-6}). Following normalization, the resulting probabilities are $p_{0,i}$ and $p_{1,i}$ for the apo and substrate-bound states, respectively, where $\sum_i^{60} p_{0,i} = \sum_i^{60} p_{1,i} = 1$, and i indexes the bins. Thus, the system has 120 bins, or microstates: 60 in the bound microstate, and 60 in the apo microstate.

We then converted these probability distributions into bin-dependent standard chemical potentials $\mu_{x,i}$, adjusted to account for the experimentally known dissociation constant of the substrate K_d. Start with preliminary definitions of the chemical potentials, as follows:

$$\mu_{x,i} = -RT \ln p_{x,i} \tag{1}$$

$$\mu_x = -RT \ln \sum_{i=1}^{60} \exp(-\beta \mu_{x,i}) = -RT \ln \sum_{i=1}^{60} p_{x,i} = 0$$

where R is the gas constant, T is the absolute temperature, $\beta \equiv (RT)^{-1}$, and $x = 0$ in the apo state and $x = 1$ in the bound state. Using these definitions, the bound and free states have equal chemical potentials of zero, which is, in general, incorrect. We therefore derived a uniform energy offset between the two energy surfaces so that the resulting differences in standard chemical potential yield the correct value of K_d. We arbitrarily chose the apo state surface as the one that will be adjusted, leaving the bound surface unchanged. Thus, using m to indicate the modified surface, we have

$$\mu_{0,i}^m = \mu_{0,i} + \mu_{\text{offset}}. \tag{2}$$

It follows that

$$\mu_0^m = \mu_{\text{offset}}. \tag{3}$$

The offset is derived as follows. From thermodynamics, we have:

$$\frac{p_1}{p_0} = \frac{Cp_1}{Cp_0} = \frac{C_1}{C_0} = C_S K_{\text{d}}^{-1} \tag{4}$$

$$= C_S \exp\{-\beta(\mu_1^m - (\mu_0^m + \mu_S^0))\} = C_S \exp\{-\beta(\mu_{\text{offset}} + \mu_S^0)\}$$

$$= \exp(-\beta \mu_{\text{offset}}^*)$$

$$\mu^*_{\text{offset}} = \mu_{\text{offset}} + \mu^0_{\text{S}} = -RT \ln K_{\text{d}}.$$

Here C_S is the concentration of substrate; C_1 and C_0 are the concentration of the bound and apo states of the protein, respectively, and C is the total concentration of protein; p_1 and p_0 are the probabilities that a given enzyme molecule is in the bound or apo state, respectively; and μ^0_{S} is the standard chemical potential of the substrate. In the last equality, recognizing that we do not have a value for the standard chemical potential of the substrate, but that it is a constant for each enzymatic reaction, we combine it with the initial offset, to obtain a new effective offset μ^*_{offset}, to be used in place of μ_{offset} in equations (2) and (3). The second line in equation (4) gives a physical interpretation of μ^*_{offset}, as well as a practical expression for evaluating it in terms of the known dissociation constant of the substrate and the enzyme. We can now write what we may be termed the "effective chemical potentials," which are used in the kinetic model below, as

$$\mu^{\text{effective}}_{0,i} = \mu_{0,i} - RT \ln K_{\text{d}} \qquad (5)$$

$$\mu^{\text{effective}}_{1,i} = \mu_{1,i}.$$

Note that the chemical potentials of the bound surface, obtained from equation (1) are used without modification. Intuitively, equation (5) means that the higher the substrate concentration, and the higher the association constant (or lower the dissociation constant), the more the apo state will be destabilized relative to the bound state. This makes sense, as both factors drive binding.

In summary, for each torsion angle analyzed, this derivation defines a system with one torsional energy surface for the set of bound microstates and another for the set of apo microstates (Fig. 3b,f and S1). The torsion angle is discretized into 60 bins, so there are 120 bins in total. The energy (chemical potential) in each bin is chosen to replicate the equilibrium torsional

distributions obtained from MD, while the equilibrium distribution between the two macrostates is appropriate to the assumed concentration of substrate and its experimentally measured dissociation constant.

Assignment of rate constants

When the system is in bin i of surface $x = 0$ or $x = 1$, it can transition either to a neighboring bin on the same surface, $i \rightarrow i - 1$ or $i \rightarrow i + 1$ with x constant (Fig. S1, arrows 1-8) or to the corresponding bin on the other surface, so that x changes from $0 \rightarrow 1$ or $1 \rightarrow 0$ with i constant (Fig. S1, arrows 9-11). Transitions between neighboring bins on each energy surface are modeled by first order rate processes, with the rate constants chosen to replicate free rotational diffusion in the limit of a flat energy surface. Thus, the rate constants for the $i \rightarrow i + 1$ and $i + 1 \rightarrow i$ intrasurface transitions are given by:

$$k_{0,i\rightarrow i+1} = D \exp\left\{-\frac{\left(\mu_{0,i+1}^{\text{effective}} - \mu_{0,i}^{\text{effective}}\right)}{2RT}\right\} \tag{6}$$

$$k_{0,i+1\rightarrow i} = D \exp\left\{-\frac{\left(\mu_{0,i}^{\text{effective}} - \mu_{0,i+1}^{\text{effective}}\right)}{2RT}\right\}$$

$$k_{1,i\rightarrow i+1} = D \exp\left\{-\frac{\left(\mu_{1,i+1}^{\text{effective}} - \mu_{1,i}^{\text{effective}}\right)}{2RT}\right\}$$

$$k_{0,i+1\rightarrow i} = D \exp\left\{-\frac{\left(\mu_{1,i}^{\text{effective}} - \mu_{1,i+1}^{\text{effective}}\right)}{2RT}\right\}$$

The forward and reverse rate constants are equal to D if the energy difference between the two bins is zero, and an energy difference increases and decreases the forward and reverse rate constants, respectively, by the same factor, as expected on physical grounds. The choice of D is discussed in Assignment of Numerical Parameters, below.

Transitions between the surfaces at the same bin, i.e., substrate binding and dissociation, are accounted for with rate constants that yield equal occupancy of both protein states when the substrate concentration equals its experimental dissociation constant (Fig. S1, arrows 9 and 10). Transitions from the bound to the apo state can also occur by a first order catalytic step (Fig. S1, arrow 11), with a rate constant based on the experimental k_{cat}.

The transitions from the apo to the bound state result from the binding of substrate, and the rate is proportional to the concentration of substrate C_S. Here, we assign an effective first-order rate constant for such transitions that includes the substrate concentration, and is independent of bin,

$$k_{0\to 1,i} = k_{\text{on}} C_S. \tag{7}$$

The dissociation rate constant depends on the energy difference between the apo and bound surfaces at that bin, so that, in the absence of catalysis, the correct equilibrium is established between the bound and apo states. Catalytic conversion of the substrate to product provides a second mechanism for the transition from bound to apo, with a constant k_{cat} assumed uniform across bins. The combination of dissociation and catalysis yields a transition rate constant in bin i of

$$k_{1\to 0,i} = k_{\text{on}} \exp\left\{-\frac{\left(\mu_{0,i}^{\text{effective}} - \mu_{1,i}^{\text{effective}}\right)}{RT}\right\} + k_{\text{cat}}. \tag{8}$$

Steady-state solution of the kinetic model

The system of rate equations is discretized by multiplying each intrasurface and intersurface rate constant by a small time interval dt, yielding the fractional change in probability within each bin over this time. From these values, we construct a 120×120 Markov transition matrix with elements that contain these fractional probability changes. The diagonal entries are determined from the requirement that the sum of each row in the matrix equals 1. We used numerical

methods (*31, 32*) to diagonalize the matrix, and the eigenvector whose corresponding eigenvalue value is unity corresponds to the steady state populations, $p_{x,i}^{\mathrm{ss}}$ of all 120 bins in the system. The steady state probability flux between bins i and $i+1$ on surface x is then

$$J_{x,i} = p_{x,i}^{\mathrm{ss}} k_{x,i\to i+1} - p_{x,i+1}^{\mathrm{ss}} k_{x,i+1\to i}. \tag{9}$$

The net probability flux is simply the sum across both surfaces,

$$J_i = \left(p_{0,i}^{\mathrm{ss}} k_{0,i\to i+1} - p_{0,i+1}^{\mathrm{ss}} k_{0,i+1\to i}\right) + \left(p_{1,i}^{\mathrm{ss}} k_{1,i\to i+1} - p_{1,i+1}^{\mathrm{ss}} k_{1,i+1\to i}\right). \tag{10}$$

In general, J_i is uniform across bins and we write $J \equiv J_i$ in the main text as "directional flux". We also report "reciprocating flux" for each torsion as the peak magnitude of directional flux across either surface, $J_R = \max\left(|J_{0,i}|, |J_{1,i}|\right)$.

Applying a load (torque) to a torsion angle

One test of these motors is their ability to do work against a mechanical load. We apply the load by tilting the free energy surfaces with a constant slope, corresponding to a torque, τ, that opposes the direction of flux. This is done by supplementing the chemical potential differences in equation (5) with an energy difference ΔE, to generate rate expressions of the form

$$k_{0,i\to i+1} = D \exp\left\{-\frac{\left(\mu_{0,i+1}^{\mathrm{effective}} - \mu_{0,i}^{\mathrm{effective}} + \Delta E\right)}{2RT}\right\} \tag{11}$$

$$k_{0,i+1\to i} = D \exp\left\{-\frac{\left(\mu_{0,i}^{\mathrm{effective}} - \mu_{0,i+1}^{\mathrm{effective}} - \Delta \mathrm{E}\right)}{2RT}\right\}$$

$$k_{1,i\to i+1} = D \exp\left\{-\frac{\left(\mu_{1,i+1}^{\mathrm{effective}} - \mu_{1,i}^{\mathrm{effective}} + \Delta E\right)}{2RT}\right\}$$

$$k_{0,i+1\to i} = D \exp\left\{-\frac{\left(\mu_{1,i}^{\mathrm{effective}} - \mu_{1,i+1}^{\mathrm{effective}} - \Delta E\right)}{2RT}\right\}$$

on both energy surfaces. That is, the energy difference between adjacent bins used to compute the transition rates (equation (6)) are modified by a factor $\pm\Delta E$, depending on direction. Here

$\Delta E > 0$ gives a negative torque and is used to oppose positive probability flux. Note that, although the unloaded free energy surfaces are periodic, such that $-\pi$ and $+\pi$ are treated equivalently, we want the load to continue acting through the periodic boundary. This is accomplished by replacing $\mu_{x,1} - \mu_{x,60}$ with $\mu_{x,1} - \mu_{x,60} + \Delta E$ and $\mu_{x,60} - \mu_{x,1}$ with $\mu_{x,60} - \mu_{x,1} - \Delta E$ to calculate the intrasurface rates at the periodic boundary. The stall torque is the load that brings the next flux to zero; increasing the torque beyond this limit will cause the motor to run backwards. We identify the stall torque by solving the kinetic system iteratively for a systematic scan of applied torques. The power produced is given by $P = \tau J_\tau$, where J_τ is the flux computed for a given applied torque τ. Empirically, the maximum power is found to occur at half the stall torque.

Assignment of numerical parameters

The present model requires numerical values of D, which is assumed equal across all torsions, as well as k_{on}, $K_{\mathrm{d}} = 1/K_{\mathrm{a}}$, and k_{cat} for each enzyme. An initial estimate of D was made by averaging the angular diffusion of the central C-C-C-C torsion in butane over a hundred, 1 ns Langevin dynamics simulations, with the force field torsion and nonbonded terms set to zero (i.e., with no barrier to rotation). This led to a value of 3×10^{15} degree^2 s^{-1} for D. However, this large value led to numerical instability during diagonalization of the transition matrix. We therefore tested the sensitivity of the kinetic model's results to the value of this parameter, and found that they become insensitive to the value of D as it rises above $\sim 10^9$ degree^2 s^{-1}. We used $D = 3\times10^{12}$ degree^2 s^{-1} for the present calculations, as this is well into the regime where the results are independent of D, but not so large as to cause numerical problems. The enzyme kinetic parameters and their basis in the experimental literature are provided in Table S1.

Materials and Methods:

Torsion potentials of mean force from molecular dynamics simulations

Adenylate Kinase

PDB accession 4AKE (*33*) was used as a starting structure for apo ADK; crystallographically ordered water molecules were retained. Hydrogens were added with `pdb2pqr` (*34*) at pH 7.0, bringing the net charge of the protein to -4. The substrate-bound protein was similarly modeled using PDB accession 3HPQ (*35*), which includes the ligand AP5A, a transition state analog, bound to the active site. AP5A carries a charge of -5 on the five phosphate groups, and the protein again carries a charge of -4 in the bound state. Partial atomic charges for AP5A were determined using the AM1-BCC method (*36*) in the `antechamber` program, and the remaining force field parameters were assigned from GAFF (*37, 38*). The apo and substrate-bound simulation systems were neutralized with 4 and 9 sodium ions, respectively. Both protein structures were solvated in a truncated octahedron with 12 Å padding.

Each system was energy-minimized for 20,000 steps, thermalized to 300 K over 1 ns, and equilibrated for 100 ns. Production simulations were then carried out for 1.0 μs using PME electrostatics with a 9 Å cutoff, and hydrogen mass repartitioning (*39*) with a 4 fs time step, using `pmemd.cuda.MPI` module of Amber 16 (*40*). Histograms (60 bins) of the torsion types listed in Table S2 were computed over the entire production simulation, using the `cpptraj` module (*41*) of Amber 16.

HIV Protease

PDB accession 1HHP (*42*) was used to model the apo structure of HIV-1 protease; crystallographically ordered waters were retained. To be consistent with Uniprot P03367, we made the following computational mutations: K14R, S37N, R41K, L63P, and I64V. Hydrogens were added with `pdb2pqr` at pH 7.0, bringing the net charge of the protein to +4. The substrate-

bound protein was modeled using PDB accession 1KJF (*43*) with 10 residues of the Gag protein co-crystallized (RPGNFLQSRP; residues 443-452; fragment p1-p6 or SP2-p6). The following mutations were made to make the apo and bound structures consistent: K7Q and N25D. The charge of the bound protein and peptide was +6. Both models were solvated in a truncated octahedron with 12 Å padding and 4 or 6 chloride ions, respectively, added to neutralize the charge. The simulation procedures were identical to those for ADK.

Protein Kinase A

Simulations were carried out as described in reference (*17*).

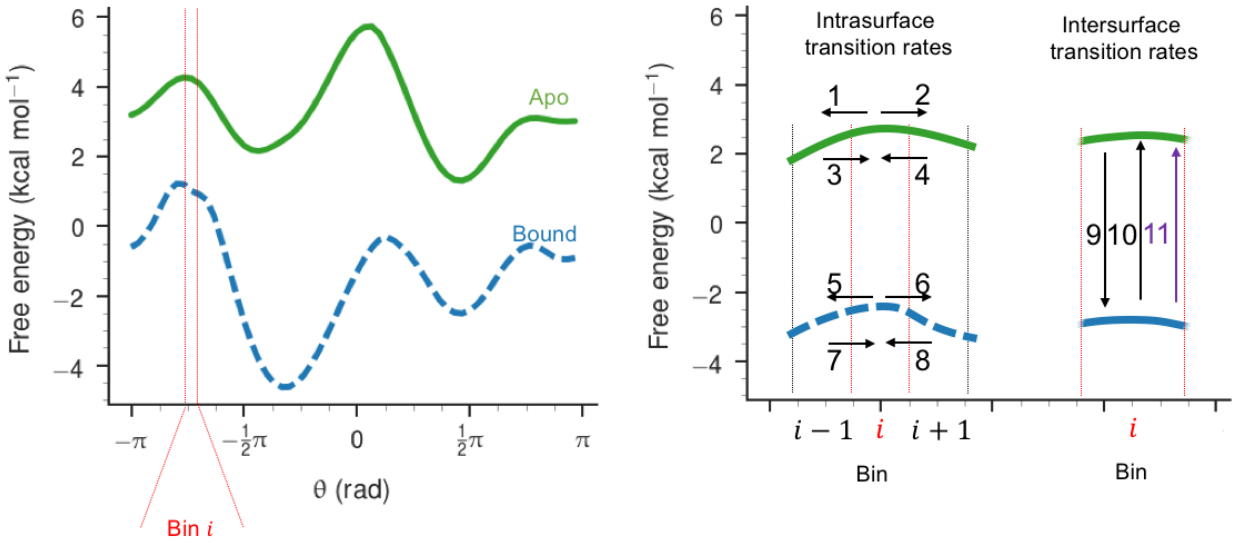

Fig. S1. Transitions in the kinetic model. Small segments of the apo (green) and bound (blue) surfaces are diagrammed, with boundaries between discretization bins denoted with vertical lines. For each bin i, there are transitions in both directions between i and $i-1$ (arrows 1 and 3) as well as between i and $i+1$ (arrows 2 and 4) on the apo surface; there are similar transitions on the bound surface (arrows 5 and 7 and arrows 6 and 8, respectively). In addition, for each bin i, there is a transition from the apo surface to the bound surface (arrow 9, substrate binding) a dissociative transition from the bound surface to the apo surface (arrow 10), and a catalytic transition from the bound surface to the apo surface (arrow 11).

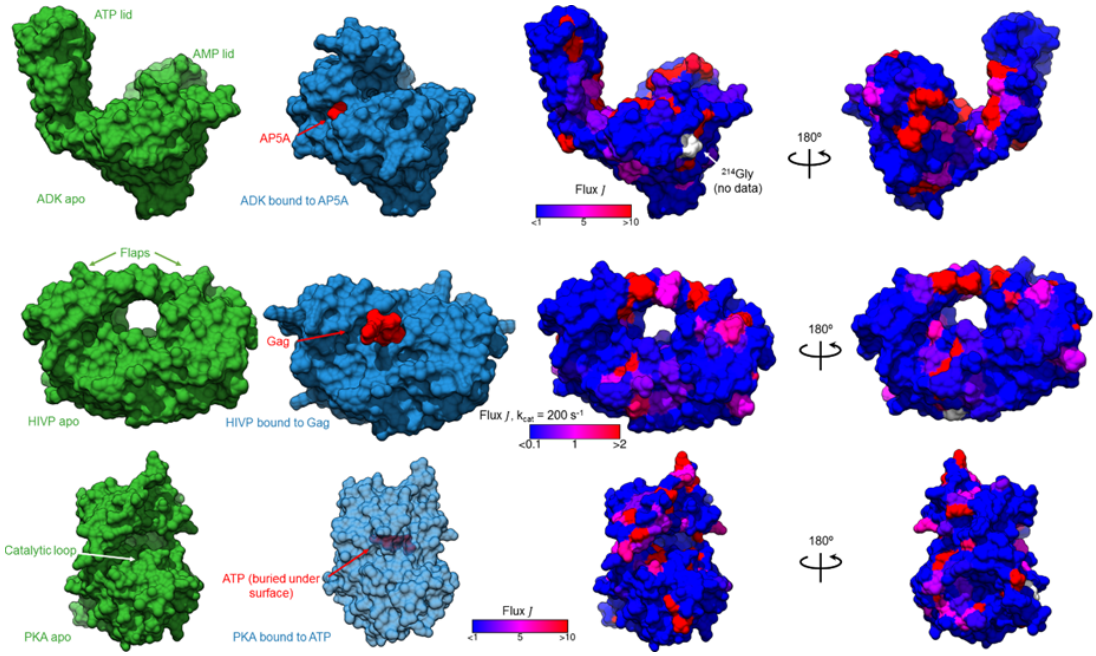

Fig. S2. The apo and substrate-bound structures of the enzymes studied. Top row: the apo (green; PDB accession 4AKE) and substrate-bound (blue; PDB accession 3HPQ) conformations of ADK, rendered as a surface, with substrate AP5A (red) as spheres. In the right two panels, the absolute magnitude of directional flux J is mapped onto the apo structure, using a color gradient with thresholds from < 1 cycle s^{-1} (blue) to > 10 cycle s^{-1} (red). Middle row: the apo (green; PDB accession 1HHP) and substrate-bound (blue; PDB accession 1KJF) conformations of HIVP, rendered as a surface, with substrate Gag peptide (red) as spheres. In the right two panels, the absolute magnitude of directional flux J is mapped onto the apo structure, using the same color gradient, with thresholds < 0.1 cycle s^{-1} (blue) to > 2 cycle s^{-1} (red), to account for the lower level of directional flux in HIVP, even at $k_{cat} = 200$ s^{-1}. Bottom row: the apo (green; PDB accession 1CMK) and substrate-bound (blue; PDB accession 3FJQ), with ATP (red) as spheres. In the right two panels, the absolute magnitude of directional flux J is mapped onto the apo structure, using the same thresholds as for ADK.

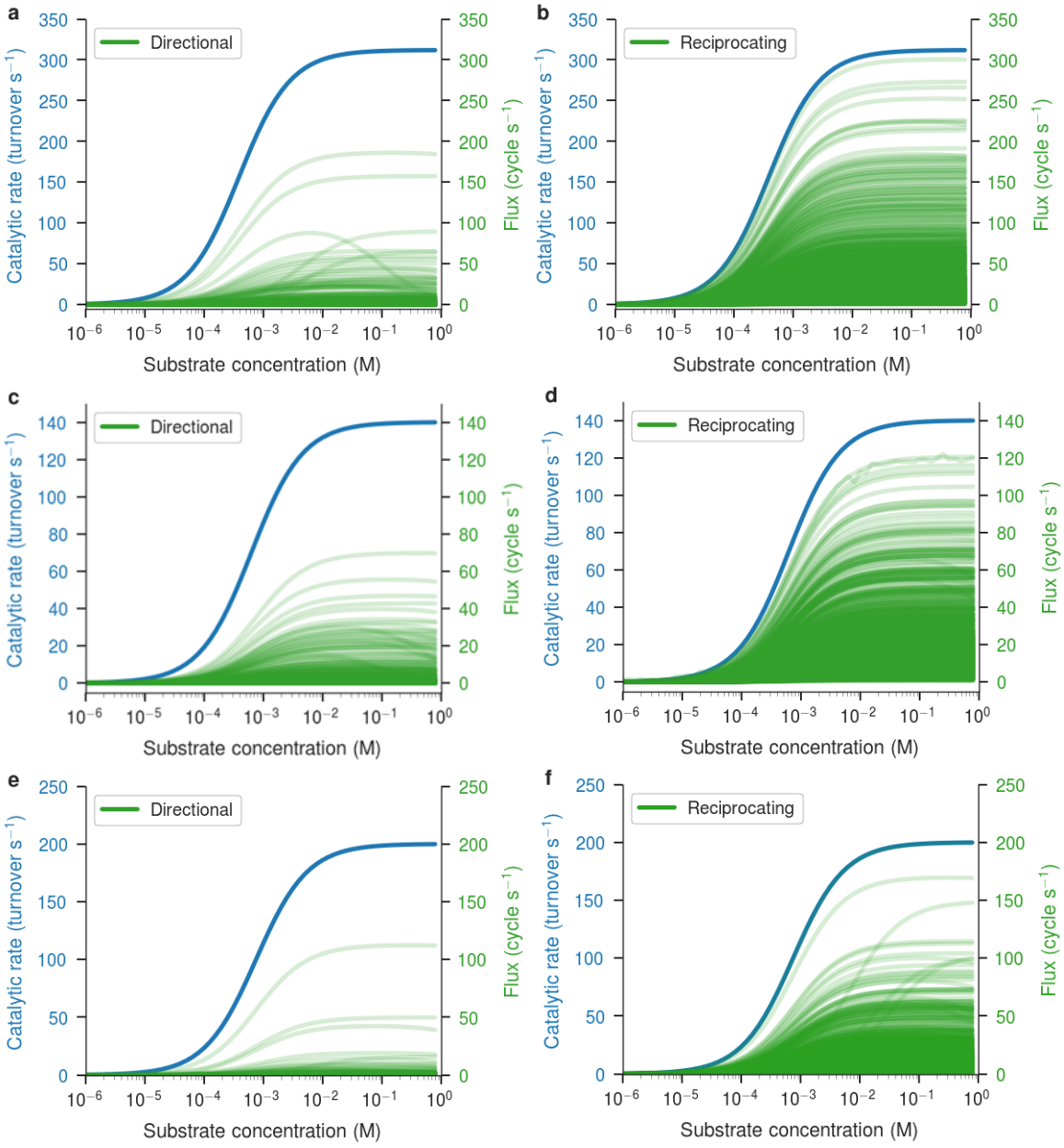

Fig. S3. The dependence of the catalytic rate (blue) and flux (green) on substrate concentration. (a-b) All angles in ADK, calculated with k_{cat} = 312 s^{-1}. (c-d) All angles in PKA, calculated with k_{cat} = 140 s^{-1}. (e-f) All angles in HIVP, calculated with k_{cat} = 200 s^{-1}. Reciprocating flux is shown only for angles with a maximum directional flux below 1 cycle s^{-1}.

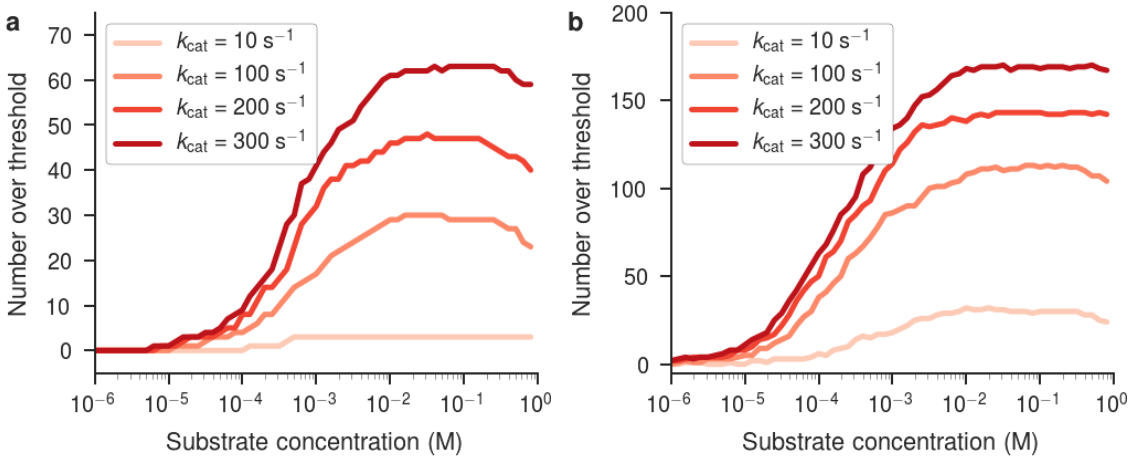

Fig. S4. Number of HIVP torsion angles with net flux magnitude, $|J|$, above a given threshold, as a function of substrate concentration, for various assumed values of k_{cat}. (a) The number of torsions with $|J| > 1$ cycle s^{-1} (b) The number of torsions with $|J| > 0.1$ cycle s^{-1}.

Table S1. Values of enzymatic parameters used in the present calculations.

	K_d (M)	μ^*_{offset} (kcal mol^{-1})	k_{on} (M^{-1} s^{-1})	k_{cat} (s^{-1})
PKA	4.0×10^{-5} [a]	-6.0	2.4×10^{6} [b]	140 [c]
ADK	6.8×10^{-5} [d]	-5.7	10^{6} [e]	312 [f]
HIV PR	5.3×10^{-4} [g]	-4.5	10^{6} [h]	10 [i]

[a] K_d for ATP in Scheme 4 in (*23*).
[b] k_1 in Scheme 4 in (*23*).
[c] The kinetics of PKA are complex and depend on, among other factors, the presence of divalent ion species and occupancy in the active site. The observed catalytic rate includes two or more conformational changes and lies between 50 s^{-1} and a fast, burst-phase of 500 s^{-1}. We used the rate-limiting step (ADP · P_i release) from Figure 11 of (*16*) in this manuscript.
[d] An average of K_d values for ATP found in (*15*) and (*44*). The calculated μ_{offset} is an average of the μ_{offset} for each K_d. The K_d values for AMP are roughly four times as large. Our model implicitly assumes a single substrate and single on rate.
[e] An order of magnitude estimate calculated using K_M from (*12*), k_{cat} values from (*12*) and (*13*), with the median expected ATP k_{off} from (*15*), and using the relationship $k_{on} = \frac{k_{off} + k_{cat}}{K_M} = (4.2 \text{ to } 5.7) \times 10^6$ M, assuming Michaelis-Menten kinetics.
[f] An average of k_{cat} from (*12*) and (*13*).
[g] A literature value of K_d for the specific Gag fragment used in the simulations was not found in the literature. However, reference (*45*) reports $K_M = 5.3 \times 10^{-4}$ M for the p1/p6 substrate sequence `PGNFLQS` (the simulated bound peptide sequence was `RPGNFLQSRP`) and for sufficiently small catalytic rate, $K_d \sim K_M$. Several other references list values for k_{cat} / K_M.
[h] No value could be found in the literature, so the same order of magnitude as ADK is used.
[i] Catalytic rates as low as 0.3 s^{-1} are reported in (*45*) for the p1/p6 substrate sequence, but other Gag sequences have catalytic rates on the order of 10 s^{-1}, see for example (*18-20*).

Table S2. Torsion angle definitions, using atom types from Amber ff14SB.

Residue	Angle	Atom 1	Atom 2	Atom 3	Atom 4
ALA	phi	C	N	CA	C
ALA	psi	N	CA	C	N
ALA	chi1	HB1	CB	CA	N
ARG	phi	C	N	CA	C
ARG	psi	N	CA	C	N
ARG	chi1	CG	CB	CA	N
ARG	chi2	CD	CG	CB	CA
ARG	chi3	NE	CD	CG	CB
ARG	chi4	CZ	NE	CD	CG
ARG	chi5	NH1	CZ	NE	CD
ASN	phi	C	N	CA	C
ASN	psi	N	CA	C	N
ASN	chi1	CG	CB	CA	N
ASN	chi2	ND2	CG	CB	CA
ASP	phi	C	N	CA	C
ASP	psi	N	CA	C	N
ASP	chi1	CG	CB	CA	N
ASP	chi2	OD2	CG	CB	CA
CYS	phi	C	N	CA	C
CYS	psi	N	CA	C	N
CYS	chi1	SG	CB	CA	N
CYS	chi2	HG	SG	CB	CA
GLN	phi	C	N	CA	C
GLN	psi	N	CA	C	N
GLN	chi1	CG	CB	CA	N
GLN	chi2	CD	CG	CB	CA
GLN	chi3	NE2	CD	CG	CB
GLN	chi4	HE21	NE2	CD	CG
GLU	phi	C	N	CA	C
GLU	psi	N	CA	C	N
GLU	chi1	CG	CB	CA	N
GLU	chi2	CD	CG	CB	CA
GLU	chi3	OE1	CD	CG	CB
GLY	phi	C	N	CA	C
GLY	psi	N	CA	C	N
HIS	phi	C	N	CA	C
HIS	psi	N	CA	C	N
HIS	chi1	CG	CB	CA	N
HIS	chi2	CD2	CG	CB	CA
ILE	phi	C	N	CA	C
ILE	psi	N	CA	C	N

```
ILE     chi1    CG1     CB      CA      N
ILE     chi2    CD1     CG1     CB      CA
LEU     phi     C       N       CA      C
LEU     psi     N       CA      C       N
LEU     chi1    CG      CB      CA      N
LEU     chi2    CD1     CG      CB      CA
LYS     phi     C       N       CA      C
LYS     psi     N       CA      C       N
LYS     chi1    CG      CB      CA      N
LYS     chi2    CD      CG      CB      CA
LYS     chi3    CE      CD      CG      CB
LYS     chi4    NZ      CE      CD      CG
MET     phi     C       N       CA      C
MET     psi     N       CA      C       N
MET     chi1    CG      CB      CA      N
MET     chi2    SD      CG      CB      CA
MET     chi3    CE      SD      CG      CB
PHE     phi     C       N       CA      C
PHE     psi     N       CA      C       N
PHE     chi1    CG      CB      CA      N
PHE     chi2    CD1     CG      CB      CA
PRO     phi     C       N       CA      C
PRO     psi     N       CA      C       N
PRO     chi1    CG      CB      CA      N
PRO     chi2    CD      CG      CB      CA
PRO     chi3    N       CD      CG      CB
SER     phi     C       N       CA      C
SER     psi     N       CA      C       N
SER     chi1    OG      CB      CA      N
THR     phi     C       N       CA      C
THR     psi     N       CA      C       N
THR     chi1    CG2     CB      CA      N
THR     chi2    HG1     OG1     CB      CA
TRP     phi     C       N       CA      C
TRP     psi     N       CA      C       N
TRP     chi1    CG      CB      CA      N
TRP     chi2    CD1     CG      CB      CA
TYR     phi     C       N       CA      C
TYR     psi     N       CA      C       N
TYR     chi1    CG      CB      CA      N
TYR     chi2    CD1     CG      CB      CA
TYR     chi3    HH      OH      CZ      CE1
VAL     phi     C       N       CA      C
```

VAL	psi	N	CA	C	N
VAL	chi1	CG1	CB	CA	N

References and Notes:

1. H. S. Muddana, S. Sengupta, T. E. Mallouk, A. Sen, P. J. Butler, Substrate catalysis enhances single-enzyme diffusion. *J. Am. Chem. Soc.* **132**, 2110-2111 (2010).
2. S. Sengupta *et al.*, Enzyme molecules as nanomotors. *J. Am. Chem. Soc.* **135**, 1406-1414 (2013).
3. C. Riedel *et al.*, The heat released during catalytic turnover enhances the diffusion of an enzyme. *Nature* **517**, 227-230 (2015).
4. R. D. Astumian, Thermodynamics and kinetics of a Brownian motor. *Science* **276**, 917-922 (1997).
5. R. D. Astumian, M. Bier, Fluctuation driven ratchets: Molecular motors. *Phys Rev Lett* **72**, 1766-1769 (1994).
6. E. R. Kay, D. A. Leigh, F. Zerbetto, Synthetic molecular motors and mechanical machines. *Angew Chem Int Ed Engl* **46**, 72-191 (2007).
7. H. Wang, G. Oster, Ratchets, power strokes, and molecular motors. *Applied Physics A* **75**, 315-323 (2002).
8. R. D. Astumian, Optical vs. chemical driving for molecular machines. *Faraday Discuss.*, (2016).
9. R. D. Astumian, Stochastic conformational pumping: a mechanism for free-energy transduction by molecules. *Annu Rev Biophys* **40**, 289-313 (2011).
10. R. D. Astumian, Enhanced diffusion, chemotaxis, and pumping by active enzymes: progress toward an organizing principle of molecular machines. *ACS Nano* **8**, 11917-11924 (2014).
11. P. Riemann, Brownian motors: noisy transport far from equilibrium. *Physics Reports*, (2002).
12. J. Aden, A. Verma, A. Schug, M. Wolf-Watz, Modulation of a Pre-existing Conformational Equilibrium Tunes Adenylate Kinase Activity. *J. Am. Chem. Soc.* **134**, 16562-16570 (2012).
13. M. Wolf-Watz *et al.*, Linkage between dynamics and catalysis in a thermophilic-mesophilic enzyme pair. *Nat. Struct. Mol. Biol.* **11**, 945-949 (2004).
14. M. Gerstein, G. Schulz, C. Chothia, Domain closure in adenylate kinase. Joints on either side of two helices close like neighboring fingers. *J. Mol. Biol.* **229**, 494-501 (1993).
15. J. A. Hanson *et al.*, Illuminating the mechanistic roles of enzyme conformational dynamics. *Proc Natl Acad Sci U S A* **104**, 18055-18060 (2007).
16. J. A. Adams, Kinetic and catalytic mechanisms of protein kinases. *Chem Rev* **101**, 2271-2290 (2001).
17. C. L. McClendon, A. P. Kornev, M. K. Gilson, S. S. Taylor, Dynamic architecture of a protein kinase. *Proc Natl Acad Sci U S A* **111**, E4623-4631 (2014).
18. E. M. Wondrak, J. M. Louis, S. Oroszlan, The Effect of Salt on the Michaelis Menten Constant of the Hiv-1 Protease Correlates with the Hofmeister Series. *FEBS Lett.* **280**, 344-346 (1991).

19. I. W. Windsor, R. T. Raines, Fluorogenic Assay for Inhibitors of HIV-1 Protease with Sub-picomolar Affinity. *Sci Rep* **5**, 11286 (2015).
20. J. Pokorna, J. Heyda, J. Konvalinka, Ion specific effects of alkali cations on the catalytic activity of HIV-1 protease. *Faraday Discuss* **160**, 359-370; discussion 389-403 (2013).
21. W. R. P. Scott, C. A. Schiffer, Curling of Flap Tips in HIV-1 Protease as a Mechanism for Substrate Entry and Tolerance of Drug Resistance. *Structure* **8**, 1259-1265 (2000).
22. N. Kurt, W. R. P. Scott, C. A. Schiffer, T. Haliloglu, Cooperative fluctuations of unliganded and substrate-bound HIV-1 protease: A structure-based analysis on a variety of conformations from crystallography and molecular dynamics simulations. *Proteins* **51**, 409-422 (2003).
23. J. Shaffer, J. A. Adams, An ATP-linked structural change in protein kinase A precedes phosphoryl transfer under physiological magnesium concentrations. *Biochemistry* **38**, 5572-5581 (1999).
24. A. Coskun, M. Banaszak, R. D. Astumian, J. F. Stoddart, B. A. Grzybowski, Great expectations: can artificial molecular machines deliver on their promise? *Chem Soc Rev* **41**, 19-30 (2012).
25. J. Howard, Motor Proteins as Nanomachines: The Roles of Thermal Fluctuations in Generating Force and Motion. *Seminaire Poincare*, (2009).
26. C. Bustamante, D. Keller, G. Oster, The physics of molecular motors. *Acc Chem Res* **34**, 412-420 (2001).
27. D. Keller, C. Bustamante, The mechanochemistry of molecular motors. *Biophys. J.* **78**, 541-556 (2000).
28. X. Bai, P. G. Wolynes, On the hydrodynamics of swimming enzymes. *J Chem Phys* **143**, 165101 (2015).
29. W. Hwang, C. Hyeon, Quantifying the Heat Dissipation from a Molecular Motor's Transport Properties in Nonequilibrium Steady States. *J Phys Chem Lett* **8**, 250-256 (2017).
30. E. M. Purcell, Life at Low Reynolds-Number. *American Journal of Physics* **45**, 3-11 (1977).
31. S. van der Walt, S. C. Colbert, G. Varoquaux, The NumPy Array: A Structure for Efficient Numerical Computation. *Comput Sci Eng* **13**, 22-30 (2011).
32. B. G. Olivier, J. M. Rohwer, J. H. Hofmeyr, Modelling cellular processes with Python and Scipy. *Mol. Biol. Rep.* **29**, 249-254 (2002).
33. C. W. Muller, G. J. Schlauderer, J. Reinstein, G. E. Schulz, Adenylate kinase motions during catalysis: an energetic counterweight balancing substrate binding. *Structure* **4**, 147-156 (1996).
34. S. Unni *et al.*, Web servers and services for electrostatics calculations with APBS and PDB2PQR. *J Comput Chem* **32**, 1488-1491 (2011).
35. T. P. Schrank, D. W. Bolen, V. J. Hilser, Rational modulation of conformational fluctuations in adenylate kinase reveals a local unfolding mechanism for allostery and functional adaptation in proteins. *Proc Natl Acad Sci U S A* **106**, 16984-16989 (2009).
36. A. Jakalian, B. L. Bush, D. B. Jack, C. I. Bayly, Fast, efficient generation of high-quality atomic charges. AM1-BCC model: I. Method. *Journal of Computational Chemistry* **21**, 132-146 (2000).

37. J. Wang, H. Tingjun, Application of Molecular Dynamics Simulations in Molecular Property Prediction I: Density and Heat of Vaporization. *J Chem Theory Comput* **7**, 2151-2165 (2011).
38. J. Wang, R. M. Wolf, J. W. Caldwell, P. A. Kollman, D. A. Case, Development and testing of a general amber force field. *J Comput Chem* **25**, 1157-1174 (2004).
39. C. W. Hopkins, S. Le Grand, R. C. Walker, A. E. Roitberg, Long-Time-Step Molecular Dynamics through Hydrogen Mass Repartitioning. *J Chem Theory Comput* **11**, 1864-1874 (2015).
40. R. M. B. D.A. Case, W. Botello-Smith, D.S. Cerutti, T.E. Cheatham, III, T.A. Darden, R.E. Duke, T.J. Giese, H. Gohlke, A.W. Goetz, N. Homeyer, S. Izadi, P. Janowski, J. Kaus, A. Kovalenko, T.S. Lee, S. LeGrand, P. Li, C. Lin, T. Luchko, R. Luo, B. Madej, D. Mermelstein, K.M. Merz, G. Monard, H. Nguyen, H.T. Nguyen, I. Omelyan, A. Onufriev, D.R. Roe, A. Roitberg, C. Sagui, C.L. Simmerling, J. Swails, R.C. Walker, J. Wang, R.M. Wolf, X. Wu, L. Xiao, D.M. York and P.A. Kollman, in *University of California, San Francisco*. (2016).
41. D. R. Roe, T. E. Cheatham, 3rd, PTRAJ and CPPTRAJ: Software for Processing and Analysis of Molecular Dynamics Trajectory Data. *J Chem Theory Comput* **9**, 3084-3095 (2013).
42. S. Spinelli, Q. Z. Liu, P. M. Alzari, P. H. Hirel, R. J. Poljak, The three-dimensional structure of the aspartyl protease from the HIV-1 isolate BRU. *Biochimie* **73**, 1391-1396 (1991).
43. M. Prabu-Jeyabalan, E. Nalivaika, C. A. Schiffer, Substrate shape determines specificity of recognition for HIV-1 protease: analysis of crystal structures of six substrate complexes. *Structure* **10**, 369-381 (2002).
44. J. Aden, M. Wolf-Watz, NMR identification of transient complexes critical to adenylate kinase catalysis. *J. Am. Chem. Soc.* **129**, 14003-14012 (2007).
45. M. E. Abram, University of Pittsburgh, (2005).

Acknowledgments: We thank Dr. N.-L. Huang for assistance preparing simulations on ADK and HIVP, and Drs. A. Gilson, K. Lindenberg, C. Van den Broeck, and J.A. McCammon for theoretical discussions. This work was funded in part by grant GM061300 from the National Institutes of Health (NIH). Its contents are solely the responsibility of the authors and do not necessarily represent the official views of the NIH.

The datasets generated and analyzed during the current study are available in the GitHub repository https://github.com/GilsonLabUCSD/nonequilibrium.

M.K.G. conceived and designed the project. D.R.S. implemented the model and performed the simulations. M.K.G. and D.R.S. analyzed the data and wrote the manuscript.